Remote Sensing Applications: Society and Environment 41 (2026) 101852

Contents lists available at ScienceDirect

Remote Sensing Applications: Society and Environment

journal homepage: www.elsevier.com/locate/rsase

Crop flood damage assessment integrating Sentinel-2 imagery and in situ data: the 2023 Emilia-Romagna case

Filippo Bocchino [a,*], Valeria Belloni [a], Roberta Ravanelli [e], Camillo Zaccarini [c], Mattia Crespi [a,b], Roderik Lindenbergh [d]

[a] Geodesy and Geomatics Division, Department of Civil, Constructional and Environmental Engineering (DICEA), Sapienza University of Rome, Rome, 00184, Italy
[b] Sapienza School for Advanced Studies, Sapienza University of Rome, Rome, 00185, Italy
[c] Risk Management Department, Institute of Services for Agricultural and Food Market (ISMEA), Rome, 00198, Italy
[d] Department of Geoscience and Remote Sensing, Delft University of Technology, Delft, 2628 CN, The Netherlands
[e] Geomatics Unit, Department of Geography, University of Liège, Liège, 4000, Belgium

ARTICLE INFO

Keywords:
Flood
Crop damage assessment
Sentinel-2 imagery
Google Earth Engine
Random Forest

ABSTRACT

Floods are among the most severe consequences of climate change, causing significant damage across several sectors, including agriculture. Nevertheless, the assessment of agricultural flood damage remains limited, particularly in agriculturally intensive regions where timely support is crucial. This work proposes a data-driven approach for assessing crop flood damage through a machine learning classification framework applied to features derived from Earth Observation (EO) data, trained and tested on field-level damage data collected by agronomists. Specifically, we applied a Random Forest model to classify fields into three damage classes by integrating Sentinel-2–derived indices, topographic information, and flood extent maps. The analysis focused on the flood event that struck the Emilia-Romagna region (Italy) in May 2023, one of the costliest floods globally that year. The model was trained and tested on 412 fields, achieving an overall accuracy of 0.74, with precision, recall, and F1 score of 0.75, 0.74, and 0.74, each with a standard deviation of 0.04, indicating stable model performance. The model accurately identified high-damage fields, which were characterized by greater flood exposure, lower elevations, and pronounced declines in vegetation indices. However, it struggled to distinguish between no-damage and medium-damage fields, particularly for permanent crops, where damage often occurs beneath the canopy and flooded areas may be partially occluded. The main novelty of this work lies in the use of in situ crop damage assessments, enabling a data-driven estimation of flood impacts. These results have direct implications for policymakers: the framework relies on free EO data, providing a tool that can support post-event compensation and decision-making in flood-prone regions.

1. Introduction

Climate change is profoundly impacting the Earth system, leading to an increase in the frequency and intensity of natural disasters. In 2023, floods were the most common type of disaster, with 164 events affecting approximately 32.4 million people worldwide (Anon, 2024). These events caused extensive damage to both urban and agricultural areas, resulting in significant

* Corresponding author.
E-mail address: filippo.bocchino@uniroma1.it (F. Bocchino).

https://doi.org/10.1016/j.rsase.2025.101852
Received 5 August 2025; Received in revised form 9 December 2025; Accepted 22 December 2025
Available online 31 December 2025

economic losses. While numerous studies have focused on the evaluation of flood impacts in urban environments, comprehensive frameworks for evaluating flood damage in the agricultural sector remain limited (Klaus et al., 2016; Förster et al., 2008; Tapia-Silva et al., 2011). Yet, the accurate quantification of agricultural flood damage in terms of crop losses is essential to develop effective compensation mechanisms to support affected farmers (Alam et al., 2020).

Traditionally, crop flood damage has been estimated through empirical damage curves (Dutta et al., 2003; Tapia-Silva et al., 2011; Brémond et al., 2013; Brémond and Grelot, 2010; Bubeck et al., 2011) and ex-post in situ surveys. However, these methods are limited by oversimplified assumptions, logistical constraints related to cost, time, and privacy, and inconsistent data availability, especially in remote or low-income regions (Wagenaar et al., 2016; Kellermann et al., 2020). Earth Observation (EO) technologies offer a valuable alternative to overcome these challenges (Shen et al., 2019) and have been widely used to map flooded agricultural areas (Bangira et al., 2017; Tran et al., 2022; Nhangumbe et al., 2023; Konrad et al., 2025). Yet, most of these studies focused only on delineating the extent of floods in agricultural areas, rather than quantifying the severity of the resulting damage in terms of yield losses. Some studies have attempted to estimate indirect damage by intersecting flood extent maps with land cover datasets (De Petris et al., 2021; Khatun et al., 2022; Gord et al., 2022), but these approaches only measure the spatial extent of inundation without providing a direct assessment of flood-induced crop losses. Other studies have leveraged EO data to assess flood-induced damage in agricultural fields using vegetation indices (Rahman and Di, 2020). Most of these approaches mainly rely on the Normalized Difference Vegetation Index (NDVI) and its derivatives, such as the Vegetation Condition Index (VCI), to detect pre- and post-flood variations in crop vigor for rapid damage assessment. Among these, Pantaleoni et al. (2007) employed Landsat 5 Thematic Mapper imagery to compute the NDVI difference before and after the flood that occurred in Indiana in July 2003, in order to monitor changes in crop conditions caused by the event. However, the relatively low spatial and spectral resolution of Landsat 5 limited the applicability of their results. More recently, similar vegetation index-based approaches have been widely adopted using the Moderate Resolution Imaging Spectroradiometer (MODIS) and Sentinel-2 (S2) imagery. Di et al. (2018) introduced the Disaster Vegetation Damage Index (DVDI), applied to the 2011 Missouri River flood in Iowa (USA) and the 2016 Louisiana flood (USA), while Wen et al. (2025) proposed the NDVI disaster level to evaluate crop impacts during the 2023 Hebei Province flood in China. These methods generally estimate damage severity through predefined index thresholds. Building on these concepts, Dang et al. (2024) developed the Crop Flood Damage Assessment Index (CFAI), which leverages weighted composite indicators to improve the robustness and sensitivity of the analysis. Their work was applied to the 2019 Missouri River floods in the United States and the 2021 Henan flood in China. Further research has also emphasized the crop-specific nature of flood impacts, with targeted studies focusing on crops such as sugarcane (Den Besten et al., 2023) and rice (Kotera et al., 2015).

Recently, Machine Learning (ML) approaches have been increasingly adopted for crop flood damage assessment. In this context, Shrestha et al. (2017) conducted a linear regression analysis to examine the relationship between NDVI dynamics and corn yield across the major corn-producing states in the U.S. Midwest during the 2000–2014 period. Lateef et al. (2025) applied a Random Forest (RF) classifier using S2 spectral variables, with training and testing samples derived from the visual interpretation of satellite imagery in Hadejia, Nigeria. However, their approach focused on mapping post-flood crop recovery levels rather than directly assessing flood-induced damage, and the georeferenced participatory mapping data collected from farmer surveys were used exclusively for validation. In contrast, Miao et al. (2023) integrated field-collected samples directly into the training and validation of an RF model, enabling direct classification of agricultural fields by damage severity in the Henan Province (China) during the 2021 flood event.

Deep Learning (DL) approaches have also been explored in this context. Lazin et al. (2021) employed a Convolutional Neural Network (CNN) to estimate the extent of cropland damaged by flooding at the county level in the U.S. Midwest, while Yang and Cervone (2019) proposed a hybrid DL and ML framework to automatically perform disaster assessment from aerial imagery. However, these models often suffered from limited interpretability, hindering a clear understanding of the factors driving the observed damage patterns. Moreover, most of them focused solely on the performance of DL methods without providing details on the case studies or the satellite data used (Liu et al., 2024; Kumar, 2025). Despite these advances, studies explicitly targeting quantitative assessment of crop flood damage using ML or DL remain limited, mainly due to the scarcity of in situ damage data (Safonova et al., 2023) and the still fragmented understanding of flood damage mechanisms in agricultural systems.

In this context, our study quantitatively assesses crop flood damage using an ML classification model applied to features derived from EO data, trained and tested on a ground truth in situ damage dataset specifically focused on agricultural flood damage assessment. The main contribution of this work lies in the integration of these field-validated records within an RF framework, enabling a data-driven evaluation of flood impacts that is directly linked to real-world observations. In details, we integrated spatial and temporal variations in spectral indices derived from S2 imagery with additional satellite-derived products, applying an RF model to classify 412 agricultural fields into three flood damage categories: no damage, medium damage, and high damage. The analysis focused on the flood event that impacted the Emilia-Romagna region (Italy) in May 2023, one of the costliest floods globally that year (Emilia-Romagna, 2025). The subsequent flooding in September and October 2024 (Copernicus, 2024c) demonstrates the persistent vulnerability of these agricultural areas to extreme events, emphasizing the necessity of robust, data-driven methods for timely and objective damage evaluation to support effective compensation strategies.

In summary, the key contributions of this study are:

- moving beyond traditional flood extent mapping to enable direct, quantitative assessment of flood-induced agricultural damage in terms of yield losses;
- training and testing an RF model on a unique in situ damage dataset;
- integrating a diverse set of features, including vegetation indices, flood extent maps, and field elevation from a Digital Elevation Model (DEM);
- providing a decision-support tool designed to address the specific monitoring challenges of flood-prone agricultural systems.

2. Study area and data

2.1. Study area

We applied the proposed methodology in Emilia-Romagna (Italy), a key region for the Italian agricultural and industrial sectors. Due to its geographical and hydrological characteristics, the area has long been exposed to flooding, with several catastrophic events in recent years (Copernicus, 2024c; CIMA, 2024; Ferrari et al., 2025). In May 2023, Emilia-Romagna was struck by two major flooding events within two weeks (CEMS, 2024). The first event took place on 2 May 2023, while the main flood event occurred between 16 May and 18 May, triggered by a persistent low-pressure system over the central Mediterranean. During this period, the region recorded precipitation levels exceeding 200 mm in 48 h, corresponding to an estimated return period of approximately 200 years (Barnes et al., 2023). Beyond the intense rainfall, two additional factors significantly amplified the impact of flooding. First, much of the region had already experienced flooding earlier in the month, which left the soil highly saturated and unable to absorb additional rain (Copernicus, 2024a). This condition increased surface runoff and rapid accumulation of water in river basins. At the same time, strong offshore winds elevated local sea levels, which hindered river outflow into the Adriatic Sea and consequently intensified flooding in coastal and low-lying areas (Carpenter, 2024). The combination of these factors created a highly critical hydrological situation, contributing to one of the most severe flood events recorded in Emilia-Romagna in recent decades.

The consequences of the flood were severe, particularly for the agricultural sector, which represents one of the economic pillars of Emilia-Romagna. More than 5000 farms in the affected areas were submerged, resulting in severe losses of crops, livestock, and agricultural infrastructure, with total damage estimated to exceed 8.5 billion euros (Emilia-Romagna, 2025). Beyond the substantial economic impact, the crisis was exacerbated by the low acceptance of flood insurance, especially within the local farming community. As a result, the costs of recovery were borne largely by individuals, local companies and public institutions (Arrighi and Domeneghetti, 2024). Fig. 1 shows the location of the study area.

2.2. Data

The input data for our study consists of remote sensing and in situ data. The remote sensing component includes multispectral S2 imagery, a DEM, and flood extent maps. As multispectral data, we used the *Harmonized Sentinel-2 MSI: MultiSpectral Instrument, Level-2A* image collection, available through Google Earth Engine (GEE) (GEE, 2024a). For elevation data, we used the NASA-developed Digital Elevation Model (NASADEM), derived from a reprocessed version of the Shuttle Radar Topography Mission (SRTM) and enhanced with elevation information from the Advanced Spaceborne Thermal Emission and Reflection Radiometer (ASTER) Global DEM (GEE, 2024c; Crippen et al., 2016). We chose NASADEM for its high spatial resolution (30 m) and fine vertical accuracy, with a reported mean vertical error of 1.51 m in flood-prone areas (Meadows et al., 2024). Finally, we obtained flood extent information from the Copernicus Emergency Management Service (CEMS), which provides freely available flood maps based on satellite imagery and geospatial data during natural disasters (CEMS, 2024). Specifically, we used two products from the CEMS Rapid Mapping activations (EMSR, Emergency Mapping Service – Rapid): EMSR659 (flood event on 2 May 2023) and EMSR664 (flood event on 16 May 2023) (Fig. 1).

In addition to remote sensing data, we incorporated in situ damage assessment data provided by the Institute of Services for Agricultural and Food Market (ISMEA) and collected during the 2023 experimental activity. This dataset includes flood damage estimates for 412 agricultural fields within the study area (Fig. 1) (ISMEA, 2022, 2023). During the campaign, flood damage was assessed by experts for each field using a standard procedure developed by ISMEA in which flood damage is defined as shown in Eq. (1) (ISMEA, 2021):

$$\text{Damage (\%)} = \frac{\text{PP} - \text{TP}}{\text{PP}} \times 100 \tag{1}$$

where PP represents the Potential Production of the crop (kg/ha × ha), while TP denotes the True Production, i.e., the actual yield at the time of harvest (kg/ha × ha). The most critical phase of this procedure is the estimation of the TP, which is defined through a sampling process. This involves selecting representative plants, verifying the total number of plants, and counting fruits that are free from diseases, defects, or other damage. The weight of these fruits is then used to estimate the TP. Therefore, selecting a truly representative sample is crucial, as this significantly affects the accuracy of the TP and the corresponding damage.

Table 1 shows the dates, spatial resolution, and reference systems for each dataset used.

3. Methodology

This section describes the workflow, which includes two steps: data pre-processing and training/testing of ML models (Fig. 2).

3.1. Data pre-processing

3.1.1. Satellite data pre-processing

We carried out data pre-processing within GEE. First, we selected S2 images collected in the EMSR664 Area Of Interest (AOI) (Fig. 1). Given the high cloud coverage observed during and immediately after the flood event, we adopted a 30% cloud cover threshold to exclude excessively cloudy scenes while maintaining an adequate temporal coverage. We further masked residual clouds and cloud shadows using the Cloud Score+ pre-processor (Pasquarella et al., 2023). After this step, we temporally filtered images

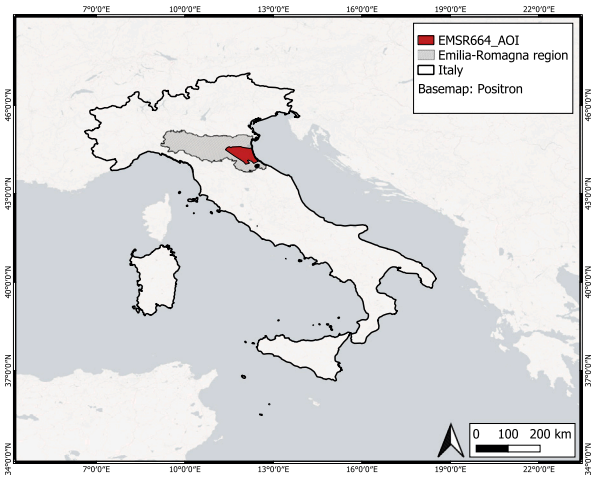

(a)

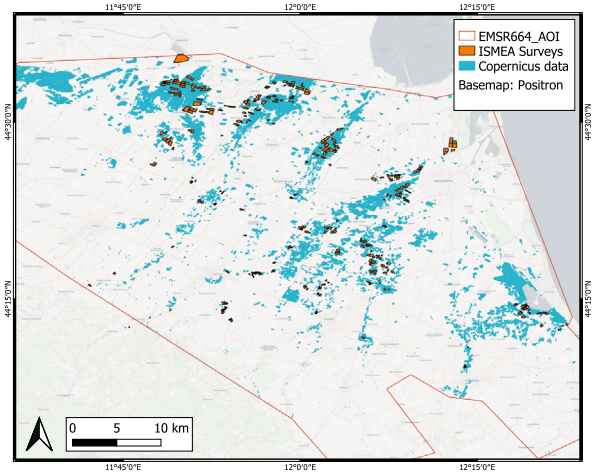

(b)

Fig. 1. Location of the study area and flood extent. (a) Map of the study area indicating the Area of Interest (AOI_EMSR664) corresponding to the flood event of 16 May 2023, as recorded by the Copernicus Emergency Management Service (CEMS). (b) CEMS Spatial extent of the flooded area (cyan), overlaid with the agricultural fields inspected during in situ damage assessments provided by the Institute of Services for the Agricultural and Food Market (ISMEA) (orange). (For interpretation of the references to color in this figure legend, the reader is referred to the web version of this article.)

between April and June 2023, and we obtained 7 images in April, 8 in May, and 14 in June (Table 1). We then processed the selected images to derive spectral indices relevant for assessing crop health and flood conditions: NDVI (Rouse Jr. et al., 1974) and Leaf Area Index (LAI) (Parker, 2020) for crop health and Modified Normalized Difference Water Index (MNDWI) (Xu, 2006) for the presence of water. These indices are closely associated with both the occurrence and severity of flood-induced agricultural damage. We computed the three indices for each S2 image and applied the median reducer to compute the monthly median image of NDVI, LAI, and MNDWI for April, May, and June ($NDVI_{April}$, $NDVI_{May}$, $NDVI_{June}$, LAI_{April}, LAI_{May}, LAI_{June}, $MNDWI_{April}$, $MNDWI_{May}$ and $MNDWI_{June}$) (Bocchino et al., 2023). We then calculated the per-pixel differences between the April and May NDVI median images, as well as between the May and June ($\Delta NDVI_{April-May}$ and $\Delta NDVI_{May-June}$ images). We applied the same procedure to the LAI and MNDWI indices, resulting in $\Delta LAI_{April-May}$, $\Delta LAI_{May-June}$, $\Delta MNDWI_{April-May}$, and $\Delta MNDWI_{May-June}$ images. We considered the spectral index variations from April to May to assess the flood impact in relation to pre-event conditions. We used May-June variations to assess post-event conditions, helping to determine whether water remained in the fields, causing prolonged damage, or whether the crops had started to recover. Finally, to spatially aggregate the temporal variations of the spectral indices at the field level, we computed the spatial median of each spectral index variation image for each analyzed field, considering

Table 1
Overview of the datasets used in the analysis, including Sentinel-2 imagery, NASADEM elevation data, Copernicus Emergency Management Service (CEMS) flood products, and ISMEA field surveys. For each dataset, dates, spatial resolution, and coordinate reference system (EPSG) are reported.

Sentinel-2 data			
Tile	Date	Spatial resolution (m)	EPSG
T32TQP	03/04/2023, 10/04/2023, 23/05/2023, 28/05/2023, 30/05/2023, 02/06/2023, 17/06/2023, 27/06/2023, 29/06/2023	10–20	32632
T32TQQ	04/04/2023, 10/04/2023, 20/04/2023, 23/04/2023, 05/05/2023, 23/05/2023, 25/05/2023, 30/05/2023, 02/06/2023, 09/06/2023, 12/06/2023, 17/06/2023, 19/06/2023, 24/06/2023, 29/06/2023	10–20	32632
T32TPQ	08/04/2023, 23/05/2023, 02/06/2023, 17/06/2023, 22/06/2023	10–20	32632
DEM			
Product	Survey date	Spatial resolution (m)	EPSG
NASADEM	11/02/2000–21/02/2000	30	4326
CEMS products			
ID	Date	Spatial resolution (m)	EPSG
EMSR659_AOI01_DEL_PRODUCT_17000_RTP_v2	04/05/2023	2.5	4326
EMSR659_AOI02_DEL_PRODUCT_8000_RTP_v2	04/05/2023	2.5	4326
EMSR659_AOI03_DEL_PRODUCT_22000_RTP_v1	04/05/2023	6	4326
EMSR659_AOI04_DEL_PRODUCT_15000_RTP_v1	04/05/2023	2.5	4326
EMSR664_AOI01_DEL_PRODUCT_120000_RTP_v1	17/05/2023	6.25	4326
EMSR664_AOI01_DEL_MONIT01_120000_RTP_v1	18/05/2023	6.25	4326
EMSR664_AOI01_DEL_MONIT02_130000_RTP_v2	20/05/2023	16	4326
EMSR664_AOI01_DEL_MONIT03_130000_RTP_v1	21/05/2023	10	4326
ISMEA surveys			
Geometry	Date	Spatial resolution (m)	EPSG
Polygons (shapefiles)	Harvest date (per product)	–	32632

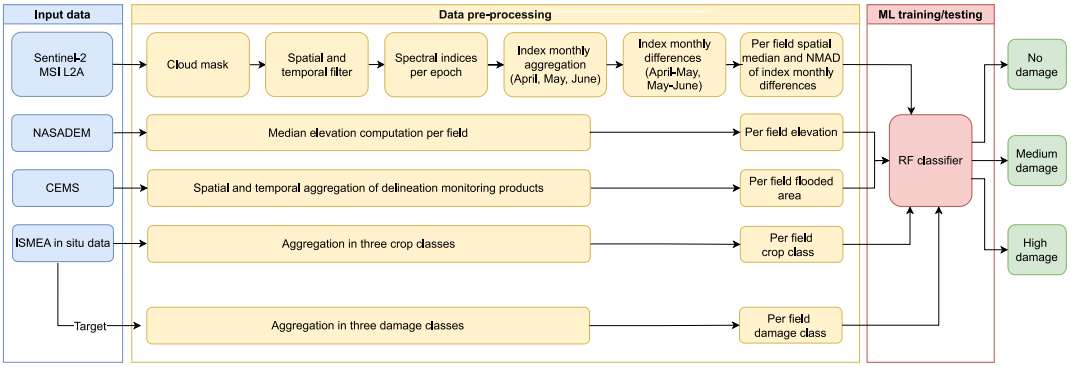

Fig. 2. Workflow of the methodology, including input data, data pre-processing for feature extraction, and machine learning model training/testing.

only the pixels within each field. Additionally, we computed the spatial Normalized Median Absolute Deviation (NMAD) (Höhle and Höhle, 2009) of the spectral index temporal variations to evaluate their spatial variability within each field.

3.1.2. Topographic and flood event data pre-processing

As a second step, we pre-processed NASADEM within GEE to derive the median elevation of each field. This information plays a crucial role in determining crop damage, as fields at higher elevations are less susceptible to flooding and prolonged water retention, which reduces the risk of water-related damage. Then, we merged all the CEMS layers related to the May 2023 flood events into a single layer that represents the total flooded area, and we calculated the percentage of water coverage for each field by dividing the flooded area by the total field area.

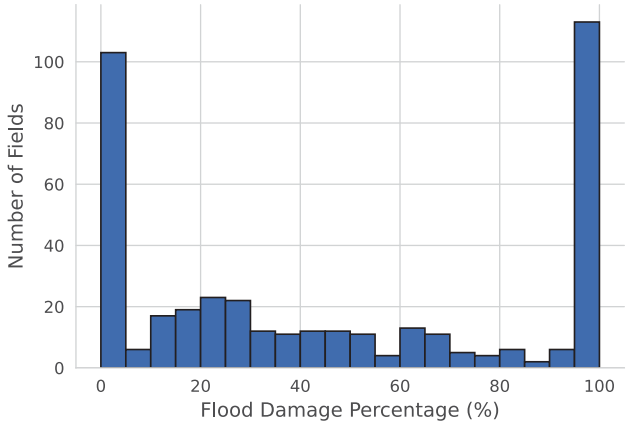

Fig. 3. Histogram of the distribution of flood damage percentages in the dataset.

Table 2
Example of the values of the features for a high-damage field.

F1	Crop class	Arable
F2	Flooded area (%)	92.29
F3	Elevation (m)	1
F4	$\Delta MNDWI_{April-May}$	−0.49
F5	NMAD $\Delta MNDWI_{April-May}$	0.03
F6	$\Delta NDVI_{April-May}$	0.36
F7	NMAD $\Delta NDVI_{April-May}$	0.03
F8	$\Delta LAI_{April-May}$	0.23
F9	NMAD $\Delta LAI_{April-May}$	0.08
F10	$\Delta MNDWI_{May-June}$	0.46
F11	NMAD $\Delta MNDWI_{May-June}$	0.03
F12	$\Delta NDVI_{May-June}$	−0.31
F13	NMAD $\Delta NDVI_{May-June}$	0.04
F14	$\Delta LAI_{May-June}$	−0.15
F15	NMAD $\Delta LAI_{May-June}$	0.07
Target	Flood damage class	High-damage (100%)

3.1.3. In situ damage data pre-processing

Finally, we pre-processed the in situ flood damage dataset. To account for the diversity of crops across surveyed fields, we categorized them into product classes according to the classification matrix developed by the Action Group on Land Monitoring in Europe (EAGLE) (Copernicus, 2024b). The EAGLE matrix is divided into three main blocks: Land Cover Components (LCC), Land Use Attributes, and Land CHaracteristics (LCH). We classified the surveyed crops into three categories: arable crops (LCH-5_1_6_1), permanent crops (LCH-5_1_6_3), and herbaceous vegetation (LCC-2_2). In total, we found that 50% of the fields were arable crops, 41% were permanent crops, and 9% were herbaceous vegetation. We then used this categorical information as an input feature for training and testing the ML models. To categorize flood damage, we also grouped fields into three classes according to their flood damage percentage ($D_{\%}$): no damage ($D_{\%} = 0\%$, 25% of the fields), medium damage ($0\% < D_{\%} \leq 60\%$, 39% of the fields), and high damage ($D_{\%} > 60\%$, 36% of the fields). We set the threshold between medium and high damage at 60%, corresponding to the median flood damage percentage of fields that experienced flood damage ($D_{\%} > 0\%$; 75% of the fields) (Fig. 3). The creation of these classes, similar to the approach adopted in Wen et al. (2025), Dang et al. (2024) and Miao et al. (2023), made it possible to build a balanced dataset.

Data pre-processing enabled us to define one target variable and fifteen input features for training and testing of ML models. Table 2 provides an example of the features (F1–F15) and the corresponding target variable for one of the fields.

3.2. ML training and testing

3.2.1. Comparison of machine learning models

We implemented the ML pipeline in Google Colaboratory (Google, 2017). To train and test ML models, we split the dataset of 412 fields into training (70%) and testing (30%), following the approach of Miao et al. (2023). We used stratified sampling to preserve the distribution of flood damage classes (Fig. 3) in both subsets. For all analyses, we normalized the input features. To ensure a more stable, unbiased, and generalizable assessment of the models under investigation, we conducted multiple independent tests using different training and testing splits. To verify the independence of the subsets across all tests, we calculated the mean

percentage of overlap among the 100 testing sets. The overlap remained below 30%, confirming that the subsets were sufficiently distinct for a reliable performance evaluation.

We compared different ML models (Arafa et al., 2024; Salem et al., 2025): RF, Gradient Boosting (GB), AdaBoost (AdaB), k-Nearest Neighbors (kNN), C-Support Vector Classification (SVC), Nu-Support Vector Classification (NuSVC), Decision Tree Classifier (DT), Gaussian Naive Bayes (GauNB), and Logistic Regression (LR). A detailed description of these algorithms can be found in Osisanwo et al. (2017).

We considered the unweighted mean F1 score per class to identify the best-performing model among the candidates, as it effectively addresses the imbalanced target classes (Bocchino et al., 2023). We repeated this procedure 100 times, and we calculated the mean and Standard Deviation (SD) of the metric across the independent tests (Bocchino et al., 2024). Then, we focused on RF (Belgiu and Drăguţ, 2016), which performed as the best model.

3.2.2. Random forest hyperparameters tuning

To optimize the RF performance, we conducted a systematic hyperparameters tuning (Probst et al., 2019), targeting different key parameters, including the maximum depth of the trees (`max_depth`), the minimum number of samples required to split an internal node (`min_samples_split`), the minimum number of samples required to be at a leaf node (`min_samples_leaf`), and the number of trees in the forest (`n_estimators`). To ensure a thorough exploration of the hyperparameter space, we tuned the hyperparameters over predefined ranges with specific step sizes. Specifically, `max_depth` was varied among {`None, 10, 20, 30`}, while `min_samples_split` and `min_samples_leaf` were adjusted from 2 to 5 and 1 to 5, respectively, with a step size of 1. The number of estimators (`n_estimators`) was tuned within the range of 75 to 400, with increments of 25. We trained and evaluated each hyperparameter combination using 50 independent training–testing subsets to reduce the computational load, and we calculated the validation metrics for each subset. We determined the optimal RF configuration by selecting the hyperparameter combination that achieved the highest mean F1 score across all 50 testing subsets.

3.2.3. Model training and validation

Finally, we trained and tested the RF model in its optimal configuration using 100 independent training and testing subsets to assess its performance. We computed the class-averaged mean and SD of the validation metrics (accuracy, precision, recall, and F1 score) across the 100 testing subsets. Then, we computed the mean confusion matrix by calculating it for each of the 100 independent tests and taking the mean values of the corresponding elements. To investigate the stability and reliability of the model's performance, we computed the SD of each element of the confusion matrix. Moreover, we analyzed feature importance across the 100 independent tests, calculating both the mean and SD. Feature importance ranked features based on their contribution to the model's predictions, with higher-ranked features indicating a greater influence on the model. Finally, since some of the analyzed features have greater "practical" or operational value (e.g., crop type) rather than environmental conditions captured by the spectral index variations, we conducted a deeper analysis on the highest-ranked feature with operational relevance to support the interpretation of potential misclassification cases.

4. Results

4.1. Feature extraction

In this section, we present the results obtained from the analysis of the features extracted after data pre-processing, which serve as inputs to the ML models. Fig. 4 shows the variations of the spectral indices between April and May, highlighting the main changes between pre- and during-event median images. Notably, the differences among the three indices show high values in the same areas, closely matching the flooded zones identified by the Copernicus flood maps (Fig. 1).

Table 3 summarizes the mean values of the main features for each flood damage class. These results provide an initial insight into feature behavior, confirming that the input variables behave as expected and are relevant to the classification task.

4.2. ML training and testing

Table 4 summarizes the performance of the tested ML models in terms of mean F1 score and SD across the 100 independent tests. Although GB, SVC, and kNN demonstrated solid performance, the RF model achieved the highest mean F1 score. Therefore, RF was selected as the best model for our classification task.

The optimal RF hyperparameter configuration, obtained from the tuning process described in Section 3.2, is: `n_estimators` = 250, `max_depth` = 20, `min_samples_leaf` = 1, and `min_samples_split` = 3. To evaluate the performance of the RF model in its optimal configuration, we computed the mean confusion matrix across 100 independent tests. The obtained confusion matrix (Fig. 5) highlights the model's ability to distinguish severely damaged fields (high-damage class) from undamaged ones (no-damage class). Nonetheless, the model faced challenges in differentiating among contiguous classes (no damage/medium damage, medium damage/high damage).

The results indicate that the RF model achieved robust performance, with class-averaged F1-score, recall, and precision, as well as overall accuracy, all further averaged over the 100 independent tests. The corresponding mean values were 0.74, 0.74, 0.75, and 0.74, respectively, each with a SD of 0.04

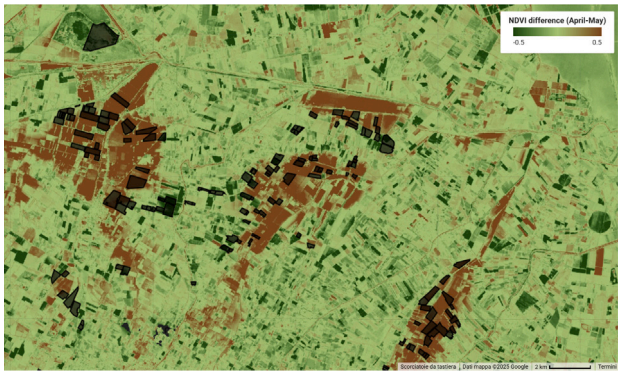

(a)

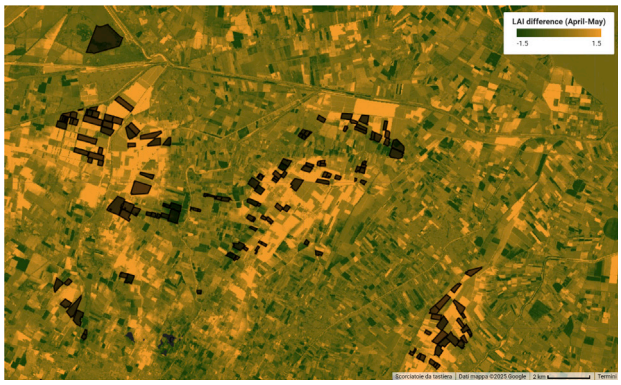

(b)

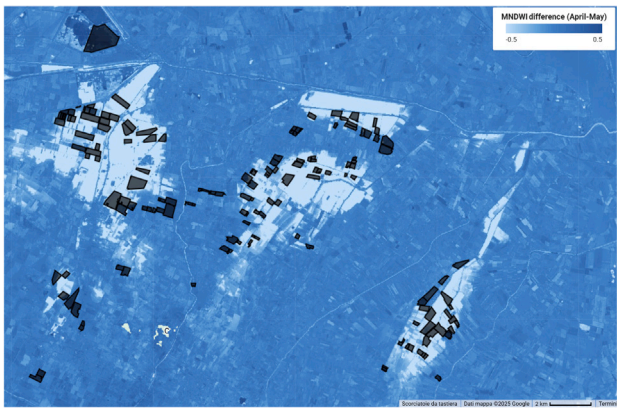

(c)

Fig. 4. $\Delta NDVI_{April-May}$ (a), $\Delta LAI_{April-May}$ (b) and $\Delta MNDWI_{April-May}$ (c) over a portion of the area of interest. Fields surveyed by ISMEA are highlighted in black.

Fig. 6 provides a spatial overview of the model's output, showing the classified fields from one of the 100 independent testing datasets and highlighting both correct and incorrect classifications.

Fig. 7 shows the mean feature importance across the 100 independent tests, along with the corresponding SD. In our analysis, the three most significant features are the flooded area, $\Delta MNDWI_{April-May}$, and crop class.

As described in Section 3.2, we further examined the highest-ranked variable with operational relevance – the crop class feature (Fig. 7) – to investigate misclassification patterns. Specifically, Table 5 summarizes how the classification results vary across the three crop types—arable crops, permanent crops, and herbaceous vegetation—showing the mean percentage of correctly and incorrectly classified fields for each crop class and flood damage class, calculated over the 100 independent tests. Misclassification between

Table 3
Mean values of main features by damage class across 412 fields. The categorical 'Crop class' feature is reported as the count of instances per damage class. N = number of fields; H = number of herbaceous crops; A = number of arable crops; P = number of permanent crops.

Features	Flood damage class		
	High-damage (N = 149)	Medium-damage (N = 160)	No-damage (N = 103)
F1: Crop class	H = 15, A = 120, P = 14	H = 20, A = 80, P = 60	H = 3, A = 7, P = 93
F2: Flooded area (%)	62.67	33.71	8.88
F3: Elevation (m)	2.42	6.56	20.96
F4: $\Delta MNDWI_{April-May}$	−0.43	−0.17	−0.04
F6: $\Delta NDVI_{April-May}$	0.33	0.05	0.00
F8: $\Delta LAI_{April-May}$	0.79	0.26	0.08
F10: $\Delta MNDWI_{May-June}$	0.39	0.14	0.07
F12: $\Delta NDVI_{May-June}$	−0.13	0.01	−0.02
F14: $\Delta LAI_{May-June}$	−0.14	−0.05	−0.19

Table 4
ML model performance evaluated using the unweighted mean F1 score per class: mean and SD across 100 independent tests.

ML model	Mean F1 score and SD
RF	0.74 ± 0.04
GB	0.71 ± 0.04
SVC	0.69 ± 0.04
kNN	0.69 ± 0.03
NuSVC	0.69 ± 0.04
LR	0.65 ± 0.04
AdaB	0.64 ± 0.04
DT	0.63 ± 0.04
GauNB	0.63 ± 0.04

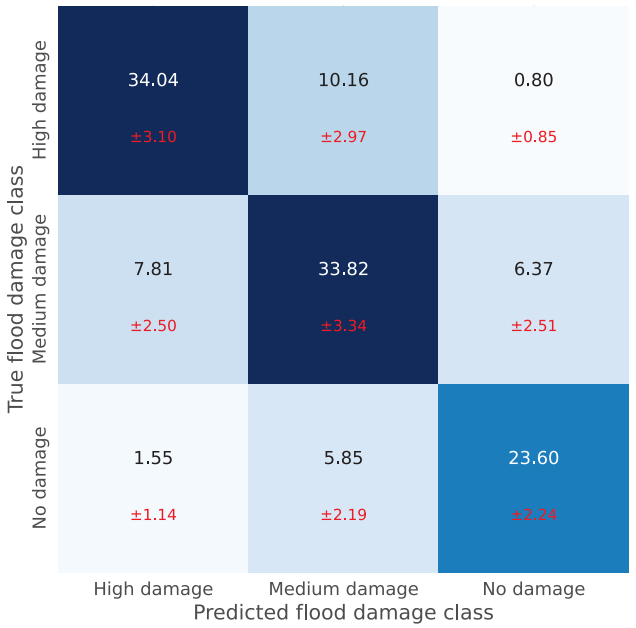

Fig. 5. Confusion matrix computed on the testing set: mean and SD of the field counts in each category over 100 independent tests.

medium-damage and no-damage fields mostly affects permanent crops (99.53% and 65.13%, respectively), while confusion between high-damage and medium-damage fields is more common in arable crops. This aligns with the high presence of arable crops in these damage classes (80% in high- and 50% in medium-damage, see Table 3). Other misclassifications, between no-damage and high-damage fields and between high-damage and no-damage fields, are much less frequent and practically negligible, each accounting for less than 1.5% of the fields.

Fig. 6. Visualization of classification results of the RF model in its best configuration for selected fields within one of 100 independent testing datasets located in the same area as Fig. 4, overlaid on the EOX::Maps - S2 cloudless basemap (EOX, 2025). Labels within misclassified fields indicate the following cases: 1 = High → Medium, 2 = High → No, 3 = Medium → High, 4 = Medium → No, 5 = No → High, 6 = No → Medium (True class → Predicted class). The labels No, Medium, and High refer to the levels of flood damage.

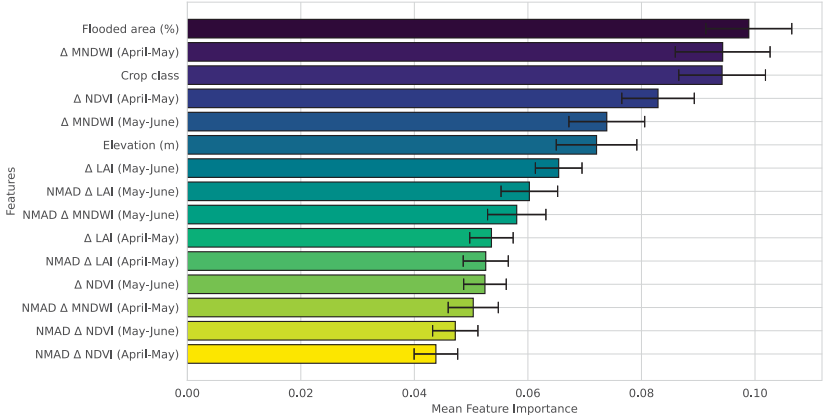

Fig. 7. Feature importance of RF model: mean and SD over 100 independent tests.

Table 5
Classification results analysis considering the three crop classes: mean percentages over 100 independent tests (T: true class, P: predicted class). The "Fields" column represents the percentage relative to the total number of fields, while the other columns indicate the percentage within each predicted class. The labels No, Medium, and High refer to the levels of flood damage.

	Fields (%)	Herbaceous vegetation (%)	Arable crops (%)	Permanent crops (%)
Correctly classified	73.76	9.03	51.43	39.54
T: No → P: Medium	4.72	8.21	26.67	65.13
T: Medium → P: No	5.14	0.00	0.47	99.53
T: Medium → P: High	6.30	23.82	63.76	12.42
T: High → P: Medium	8.19	6.10	78.74	15.16
T: No → P: High	1.25	27.74	34.84	37.42
T: High → P: No	0.65	0.00	0.00	100.00

5. Discussion

5.1. Feature extraction

The analysis of mean feature values across damage classes shown in Table 3 provides a clear picture of the physical patterns underlying flood impacts, confirming that the selected variables are meaningful and consistent for effectively discriminating between different damage levels. Focusing on the high-damage class, the $\Delta NDVI$ and ΔLAI features are positive during the April-May period, indicating higher spectral index values in the month preceding the flood (April), and, consequently, a better overall health of these fields compared to May, when the effects of the flood become evident. In contrast, $\Delta NDVI$ and ΔLAI values turn negative during the May-June period, reflecting signs of potential recovery in June. Conversely, $\Delta MNDWI$ exhibits the opposite pattern: it is negative during the April-May period and positive during the May-June period, reflecting its inverse response to water presence compared to $\Delta NDVI$ and ΔLAI. In terms of magnitude, the high-damage class is characterized by markedly different feature values compared to the medium-damage and no-damage classes. For example, the mean flooded area is 62.67% in the high-damage class, significantly higher than 33.71% in the medium-damage and 8.88% in the no-damage class. Similarly, the mean elevation is 2.42 m for high-damage fields versus 20.96 m for no-damage ones, highlighting the strong influence of topography on flood exposure. Regarding vegetation response, $\Delta NDVI$ between April and May shows a mean decrease of 0.33 in the high-damage class, compared to 0.05 in the medium and 0.00 in the no-damage class. The magnitude of ΔLAI follows the same trend, indicating a much stronger vegetation decline in the most affected areas. In contrast, $\Delta MNDWI$ between May and June reaches 0.39 in high-damage fields, more than double the value of medium-damage fields (0.14) and five times that of no-damage fields (0.07).

5.2. ML training and testing

The RF classifier in its optimal configuration demonstrated robust performance, achieving mean F1-score and precision values of 0.74 and 0.75, respectively, over 100 independent tests. Notably, all metrics converge around similar values, indicating a balanced trade-off between precision and recall across classes. Moreover, the low SD observed for all metrics highlights the stability and consistency of the model's classification performance across different tests.

A notable finding is that only a small percentage (0.65%) of high-damage fields were misclassified as undamaged, while 1.25% of undamaged fields were incorrectly classified as highly damaged (see the last two rows of Table 5). This result is particularly important for ensuring that severely damaged fields are accurately identified, minimizing the risk of overlooking those requiring high compensation. At the same time, it helps to prevent overestimation of damage in undamaged fields. However, the RF model still faces challenges in distinguishing between the no-damage and medium-damage classes (see Fig. 5). A similar issue was reported by Miao et al. (2023), who observed frequent misclassifications between adjacent damage categories. This confusion is likely related to the definition of intermediate categories in the training samples, as well as the mixed pixel effect inherent to remote sensing data, where a single pixel may cover areas with varying levels of damage. While less critical than the misclassification of high-damage/no-damage fields, the misclassification of no-damage/medium-damage fields can still lead to suboptimal resource allocation and inaccuracies in determining the necessary support for the affected farmers. Lastly, misclassification between medium-damage and high-damage occurs more frequently (6.30% and 8.19%, Table 5), though its practical impact is lower compared to the other cases.

Feature importance analysis (Fig. 7) revealed that the most significant features are: flooded area, $\Delta MNDWI_{April-May}$, crop class, $\Delta NDVI_{April-May}$, $\Delta MNDWI_{May-June}$, and elevation. The flooded area directly reflects the extent of inundation within the field, making it a key indicator of potential crop damage. The $\Delta MNDWI_{April-May}$ is particularly important, as it captures changes in surface water between the pre-flood (April) and flood (May) periods. A strong increase in MNDWI indicates water accumulation in fields, which strongly correlates with crop stress and subsequent damage. However, it is important to note that relying solely on water presence as an indicator of damage is insufficient, as discussed in De Petris et al. (2021). The crop class, ranked third, highlights how the classification results are strongly influenced by the type of crop (see also Table 5), confirming the findings of Tapia-Silva et al. (2011). For instance, permanent crops generally show greater resilience to short-term flooding compared to herbaceous or arable crops, which are more sensitive to water stress and yield losses. The $\Delta NDVI_{April-May}$ ranked fourth in feature importance, indicating that changes in vegetation vigor between pre-flood and flood conditions play a crucial role in the classification, as also emphasized by Di et al. (2018) and Wen et al. (2025). The $\Delta MNDWI_{May-June}$ further contributes valuable information, helping to distinguish between fields that remained flooded in June and those that had dried. Elevation, ranked sixth, contributes to the classification, consistent with the insights reported by Miao et al. (2023). Its slightly lower ranking is probably related to the medium spatial resolution of the NASADEM product. A higher-resolution DEM, such as the one provided by Emilia-Romagna (2019), could potentially improve classification performance. However, relying on a site-specific DEM would reduce the scalability of the methodology, reflecting the common trade-off between model performance and transferability.

Misclassifications are influenced by crop type (Table 5), which ranks third in feature importance (see Fig. 7). In particular, the medium-damage fields are more frequently misclassified as undamaged, and vice versa, in permanent crops. This finding highlights the challenge of assessing flood damage in permanent crops (e.g., fruit trees) using satellite data, as damage often affects the fruit beneath the canopy, making it difficult to detect from above (Ruiz et al., 2020). Moreover, the canopy can occlude the flooded area, potentially leading to misclassifications. Given the feature importance results (Fig. 7), this limitation may affect the model's ability to accurately differentiate among damage classes.

Finally, our study, in line with Miao et al. (2023) and Lateef et al. (2025), demonstrates that assessing damage to flood-affected cropland through an RF classification model trained on in situ survey data and fed with EO derived variables overcomes

the limitations of approaches based solely on vegetation indices. In particular, such only-index-based methods are constrained by the need to define spectral index thresholds for categorizing damage levels, which strongly depend on the specific crop and its phenological stage (Wang et al., 2021).

Traditional flood damage assessments, based on empirical damage curves, rely on generalized assumptions about hydraulic parameters and typically provide aggregated rather than parcel-level information (Brémond et al., 2013; Dutta et al., 2003). Similarly, remote sensing approaches that intersect flood extent maps with land cover data (De Petris et al., 2021; Khatun et al., 2022; Gord et al., 2022) are effective at identifying the extent of inundated agricultural areas but fail to quantify the severity of crop damage.

In this context, our approach represents an advancement by adopting an a posteriori perspective: instead of relying on predefined hydraulic or spectral thresholds, the model learns the relationship between EO-derived indicators and observed field damage levels directly from in situ data. This enables an objective, parcel-level classification of flood-affected fields into three damage categories, providing a more consistent assessment of both damage severity and spatial variability in heterogeneous agricultural landscapes.

Some uncertainties remain, mainly related to the limited availability of cloud-free S2 imagery during and after the flood, as well as the lack of detailed information on crop type and phenology. Nonetheless, although the framework is still at a preliminary stage, it could be further improved by integrating alternative ground data sources, such as crowdsourced or participatory observations (Puttinaovarat et al., 2022; Saeed et al., 2024), as well as additional features derived from Synthetic Aperture Radar data (e.g., Sentinel-1) to enhance model scalability and generalization. Once refined, the resulting field-based damage classification maps could also serve as valuable inputs for a priori flood risk analyses, supporting scenario-based assessments and contributing to a more comprehensive understanding of agricultural vulnerability and resilience to flooding (López-Andreu et al., 2022)

6. Conclusions

6.1. Main findings

By integrating spatial and temporal variations of spectral indices derived from S2 imagery, flooded area maps, elevation data, and in situ damage observations, the proposed framework goes beyond conventional flood extent mapping, enabling a detailed and quantitative evaluation of crop damage severity through an RF classification model trained and tested on in situ data.

The analysis focused on the severe flood event that struck the Emilia-Romagna region (Italy) in May 2023. We applied the RF model to classify 412 agricultural fields into three flood damage categories: no damage, medium damage, and high damage. The model achieved stable and robust classification performance (F1 score of 0.74 ± 0.04), ensuring a reliable identification of high-damage fields while minimizing misclassification in undamaged areas. Feature analysis revealed clear physical patterns across damage classes: high-damage fields were characterized by greater flood exposure, lower elevation, and pronounced declines in vegetation indices, while $\Delta MNDWI$ effectively captured water accumulation dynamics. Crop type also emerged as a key factor, reflecting the differential response of agricultural systems to flooding. Importantly, the proposed framework relies entirely on freely available EO data, ensuring its applicability to other flood events. This aligns with the objectives of the Common Agricultural Policy by supporting transparent and timely aid management.

6.2. Limitations and future work

Despite these promising results, several challenges remain. Misclassifications occurred most frequently between contiguous damage classes, reflecting their inherent ambiguity in defining and labeling intermediate damage levels in the training data. A particularly critical limitation concerns the reduced performance on permanent crops, where dense canopy cover often conceals flood impacts, leading to confusion between undamaged and moderately damaged fields. In addition, the reliance on in situ damage data from a single flood event currently limits the model's ability to generalize to other regions or events.

To address these limitations, future developments will focus on strengthening the dataset and enhancing the flexibility and transferability of the proposed workflow. First, we plan to expand the training dataset by incorporating additional ISMEA surveys collected in other flood-affected agricultural regions, thereby improving the model's robustness and generalization capability. We also aim to integrate alternative ground data sources, including crowdsourced observations gathered through user-friendly platforms, to complement traditional in situ surveys and increase spatial coverage. Furthermore, we intend to include additional features and ancillary data — such as Sentinel-1-derived water indices, soil properties, crop phenology, and weather variables — to better capture the complexity of flood–crop interactions and enhance classification performance. Finally, we plan to apply the framework to high-resolution satellite imagery, such as that expected from the upcoming International Report for an Innovative Defence of Earth (IRIDE) constellation, to improve the accuracy and detail of flood damage mapping at the field scale.

CRediT authorship contribution statement

Filippo Bocchino: Writing – review & editing, Writing – original draft, Visualization, Validation, Software, Methodology, Investigation, Formal analysis, Data curation, Conceptualization. **Valeria Belloni:** Writing – review & editing, Writing – original draft, Validation, Supervision, Methodology, Formal analysis, Conceptualization. **Roberta Ravanelli:** Writing – review & editing, Writing – original draft, Validation, Supervision, Methodology, Formal analysis, Conceptualization. **Camillo Zaccarini:** Supervision. **Mattia Crespi:** Validation, Supervision, Project administration, Methodology, Formal analysis, Conceptualization. **Roderik Lindenbergh:** Validation, Supervision, Project administration, Methodology, Formal analysis, Conceptualization.

Ethics in publishing statement

All authors agree that:

This research presents an accurate account of the work performed, all data presented are accurate and methodologies detailed enough to permit others to replicate the work.

This manuscript represents entirely original works and or if work and/or words of others have been used, that this has been appropriately cited or quoted and permission has been obtained where necessary.

This material has not been published in whole or in part elsewhere.

The manuscript is not currently being considered for publication in another journal.

All authors have been personally and actively involved in substantive work leading to the manuscript and will hold themselves jointly and individually responsible for its content.

Declaration of Generative AI and AI-assisted technologies in the writing process

The authors acknowledge the use of OpenAI,s ChatGPT (GPT-4 and GPT-5) for editing and grammar enhancement of the manuscript. The AI system was not used to generate original scientific content, analyses, figures, results or text. Its role was limited to improving clarity, readability, and consistency of the text.

Declaration of competing interest

The authors declare that they have no known competing financial interests or personal relationships that could have appeared to influence the work reported in this paper.

Acknowledgments

Filippo Bocchino was supported by the grant for young researchers AR123188B3C1EB82 and the grant for international mobility, both funded by Sapienza University of Rome, Italy, and by a Doctoral Program fellowship within the National PhD in Earth Observation funded by the Institute of Services for Agricultural and Food Market (ISMEA, Italy). The authors thank Antonio Denaro and Laura Rosatelli (ISMEA) for their valuable collaboration and support.

Data availability

The authors do not have permission to share data.

References

Alam, A.S.A.F., Begum, H., Masud, M.M., Al-Amin, A.Q., Filho, W.L., 2020. Agriculture insurance for disaster risk reduction: A case study of Malaysia. Int. J. Disaster Risk Reduct. 47, 101626. http://dx.doi.org/10.1016/j.ijdrr.2020.101626.

Anon, 2024. 2023 Disasters in Numbers. Technical Report, Centre for Research on the Epidemiology of Disasters (CRED), p. 8.

Arafa, N.A., El-Said Salem, Z., Abdeldayem, A.L., Ghorab, M.A., Moustafa, Y.M., Soliman, S.A., Farag, M.H., Purohit, S., Elhag, M., Youssef, Y.M., 2024. Advancing deltaic aquifer vulnerability mapping to seawater intrusion and human impacts in Eastern nile delta: insights from machine learning and hydrochemical perspective. Earth Syst. Environ. 1–26.

Arrighi, C., Domeneghetti, A., 2024. Brief communication: On the environmental impacts of the 2023 floods in Emilia-Romagna (Italy). Nat. Hazards Earth Syst. Sci. 24 (2), 673–679. http://dx.doi.org/10.5194/nhess-24-673-2024.

Bangira, T., Alfieri, S., Menenti, M., Van Niekerk, A., Vekerdy, Z., 2017. A spectral unmixing method with ensemble estimation of endmembers: Application to flood mapping in the Caprivi floodplain. Remote Sens. 9 (10), 1013. http://dx.doi.org/10.3390/rs9101013.

Barnes, C., Faranda, D., Coppola, E., Grazzini, F., Zachariah, M., Lu, C., Kimutai, J., Pinto, I., Pereira, C., Sengupta, S., Vahlberg, M., Singh, R., Heinrich, D., Otto, F., 2023. Limited Net Role for Climate Change in Heavy Spring Rainfall in Emilia-Romagna. Technical Report, Imperial College London, http://dx.doi.org/10.25561/104550.

Belgiu, M., Drăguţ, L., 2016. Random forest in remote sensing: A review of applications and future directions. ISPRS J. Photogramm. Remote Sens. 114, 24–31. http://dx.doi.org/10.1016/j.isprsjprs.2016.01.011, URL: https://www.sciencedirect.com/science/article/pii/S0924271616000265.

Bocchino, F., Contu, R., Ranaldi, L., Denaro, A., Rosatelli, L., Zaccarini, C., Tapete, D., Ursi, A., Virelli, M., Sacco, P., et al., 2024. Integration of remote sensing, ground data and meteo-climatic variables for agricultural drought monitoring: First results of a data-driven approach. In: IGARSS 2024-2024 IEEE International Geoscience and Remote Sensing Symposium. IEEE, pp. 1890–4894.

Bocchino, F., Ravanelli, R., Belloni, V., Mazzucchelli, P., Crespi, M., 2023. Water reservoirs monitoring through Google earth engine: Application to sentinel and landsat imagery. Int. Arch. Photogramm. Remote Sens. Spat. Inf. Sci. XLVIII-M-1-2023, 41–47. http://dx.doi.org/10.5194/isprs-archives-XLVIII-M-1-2023-41-2023.

Brémond, P., Grelot, F., 2010. Comparison of a systemic modelling of farm vulnerability and classical methods to appraise flood damage on agricultural activities. In: Adv. Sustain. in a Time of Crisis, 11th Bienn. Conf. of the Int. Soc. for Ecol. Economics, August 22–25, Oldenburg and Bremen, Germany, 2010.

Brémond, P., Grelot, F., Agenais, A.-L., 2013. Review Article: Economic evaluation of flood damage to agriculture – review and analysis of existing methods. Nat. Hazards Earth Syst. Sci. 13 (10), 2493–2512. http://dx.doi.org/10.5194/nhess-13-2493-2013.

Bubeck, P., de Moel, H., Bouwer, L.M., Aerts, J.C.J.H., 2011. How reliable are projections of future flood damage? Nat. Hazards Earth Syst. Sci. 11 (12), 3293–3306. http://dx.doi.org/10.5194/nhess-11-3293-2011.

Carpenter, G., 2024. Post event report: 2023 mid-May Emilia-Romagna flood — guycarp.com. www.guycarp.com/insights/2023/06/Italy_Emilia-Romagna_Flood_2023-05.html. (Accessed 07 September 2024).

CEMS, 2024. https://emergency.copernicus.eu/mapping/ems/emergency-management-service-mapping. (Accessed 14 September 2024).

CIMA, 2024. Flooding in Emilia-Romagna: scientific analysis by CIMA Research Foundation - CIMA Research Foundation — cimafoundation.org. https://www.cimafoundation.org/en/news/flooding-in-emilia-romagna-scientific-analysis-by-cima-research-foundation/. (Accessed 11 October 2025).

Copernicus, 2024a. Data viewer — land.copernicus.eu. https://land.copernicus.eu/en/map-viewer?dataset=0f3f3fb37eba4a12a586d1d95b3ad3fa. (Accessed 10 September 2024).

Copernicus, 2024b. EAGLE — land.copernicus.eu. https://land.copernicus.eu/en/eagle?tab=bar_coding. (Accessed 07 October 2024).

Copernicus, 2024c. Further flooding in Emilia-Romagna, Italy | Copernicus — copernicus.eu. https://www.copernicus.eu/en/media/image-day-gallery/further-flooding-emilia-romagna-italy. (Accessed 11 October 2025).

Crippen, R., Buckley, S., Agram, P., Belz, E., Gurrola, E., Hensley, S., Kobrick, M., Lavalle, M., Martin, J., Neumann, M., Nguyen, Q., Rosen, P., Shimada, J., Simard, M., Tung, W., 2016. NASADEM global elevation model: Methods and progress. Int. Arch. Photogramm. Remote Sens. Spat. Inf. Sci. XLI-B4, 125–128. http://dx.doi.org/10.5194/isprs-archives-XLI-B4-125-2016.

Dang, Y., Yang, L., Song, J., 2024. The construction of a crop flood damage assessment index to rapidly assess the extent of postdisaster impact. Remote Sens. 16 (9), http://dx.doi.org/10.3390/rs16091527.

De Petris, S., Sarvia, F., Borgogno Mondino, E., 2021. Multi-temporal mapping of flood damage to crops using sentinel-1 imagery: a case study of the Sesia River (October 2020). Remote Sens. Lett. 12 (5), 459–469. http://dx.doi.org/10.1080/2150704X.2021.1890262.

Den Besten, N., Steele Dunne, S., Mahmud, A., Jackson, D., Aouizerats, B., de Jeu, R., Burger, R., Houborg, R., McGlinchey, M., van der Zaag, P., 2023. Understanding Sentinel-1 backscatter response to sugarcane yield variability and waterlogging. Remote Sens. Environ. 290, 113555. http://dx.doi.org/10.1016/j.rse.2023.113555.

Di, L., Yu, E.G., Shrestha, R.M., Lin, L., 2018. DVDI: A new remotely sensed index for measuring vegetation damage caused by natural disasters. In: IGARSS 2018 - 2018 IEEE Int. Geosci. and Remote. Sen. Symp.. pp. 9067–9069. http://dx.doi.org/10.1109/IGARSS.2018.8518022.

Dutta, D., Herath, S., Musiake, K., 2003. A mathematical model for flood loss estimation. J. Hydrol. 277 (1), 24–49. http://dx.doi.org/10.1016/S0022-1694(03)00084-2.

Emilia-Romagna, R., 2019. DTM 5x5 — geoportale.regione.emilia-romagna.it. https://geoportale.regione.emilia-romagna.it/catalogo/dati-cartografici/altimetria/layer-2. (Accessed 12 October 2025).

Emilia-Romagna, 2025. Alluvione, un anno dopo: il primo pensiero alle vittime. Il punto su quanto fatto dalla Regione — regione.emilia-romagna.it. www.regione.emilia-romagna.it/notizie/2024/maggio/alluvione-un-anno-dopo. (Accessed 09 January 2025).

EOX, 2025. The global and cloudless Sentinel-2 map by EOX — s2maps.eu. https://s2maps.eu/. (Accessed 13 March 2025).

Ferrari, A., Passadore, G., Vacondio, R., Carniello, L., Pivato, M., Crestani, E., Carraro, F., Aureli, F., Carta, S., Stumpo, F., Mignosa, P., 2025. Brief communication: Hydrological and hydraulic investigation of the extreme September 2024 flood on the Lamone River in Emilia-Romagna, Italy. EGUsphere 2025, 1–10. http://dx.doi.org/10.5194/egusphere-2025-216.

Förster, S., Kuhlmann, B., Lindenschmidt, K.-E., Bronstert, A., 2008. Assessing flood risk for a rural detention area. Nat. Hazards Earth Syst. Sci. 8 (2), 311–322. http://dx.doi.org/10.5194/nhess-8-311-2008.

GEE, 2024a. Harmonized Sentinel-2 MSI: MultiSpectral Instrument, Level-2A — developers.google.com. https://developers.google.com/earth-engine/datasets/catalog/COPERNICUS_S2_SR_HARMONIZED. (Accessed 05 October 2024).

GEE, 2024c. NASADEM: NASA 30m Digital Elevation Model — developers.google.com. https://developers.google.com/earth-engine/datasets/catalog/NASA_NASADEM_HGT_001#description. (Accessed 12 March 2025).

Google, 2017. Google Colab — colab.research.google.com. https://colab.research.google.com/. (Accessed 12 November 2025).

Gord, S., Mavaddat, M.H., Ghobadian, R., 2022. Flood impact assessment on agricultural and municipal areas using Sentinel-1 and 2 satellite images(Case study: Kermanshah province). http://dx.doi.org/10.21203/rs.3.rs-2225762/v1, PREPRINT (Version 1) available at Research Square.

Höhle, J., Höhle, M., 2009. Accuracy assessment of digital elevation models by means of robust statistical methods. ISPRS J. Photogramm. Remote Sens. 64 (4), 398–406.

ISMEA, 2021. Progetto pilota di standardizzazione delle procedure per le valutazioni dei danni alle colture vegetali. www.ismea.it/flex/cm/pages/ServeBLOB.php/L/IT/IDPagina/11688. (Accessed 23 May 2024).

ISMEA, 2022. Sperimentazione e avviamento Fondo Agri-CAT 2022. www.ismea.it/flex/cm/pages/ServeBLOB.php/L/IT/IDPagina/12034. (Accessed 23 May 2024).

ISMEA, 2023. The National Mutual Fund against Catastrophic Events ISMEA - Report About 2022 Experimentation Activity. Technical Report, ISMEA, (Accessed 23 May 2024).

Kellermann, P., Schröter, K., Thieken, A.H., Haubrock, S.-N., Kreibich, H., 2020. The object-specific flood damage database HOWAS~21. Nat. Hazards Earth Syst. Sci. 20 (9), 2503–2519. http://dx.doi.org/10.5194/nhess-20-2503-2020.

Khatun, M., Garai, S., Sharma, J., Singh, R., Tiwari, S., Rahaman, S.M., 2022. Flood mapping and damage assessment due to the super cyclone Yaas using Google Earth Engine in Purba Medinipur, West Bengal, India. Environ. Monit. Assess. 194 (12), http://dx.doi.org/10.1007/s10661-022-10574-y.

Klaus, S., Kreibich, H., Merz, B., Kuhlmann, B., Schröter, K., 2016. Large-scale, seasonal flood risk analysis for agricultural crops in Germany. Environ. Earth Sci. 75 (18), http://dx.doi.org/10.1007/s12665-016-6096-1.

Konrad, P.M., Tanyel, T., Ayvaz, S., 2025. Beyond major floods: Deep learning for detecting shallow water inundation in agricultural areas. Procedia Comput. Sci. 270, 301–310.

Kotera, A., Nagano, T., Hanittinan, P., Koontanakulvong, S., 2015. Assessing the degree of flood damage to rice crops in the Chao Phraya delta, Thailand, using MODIS satellite imaging. Paddy Water Environ. 14 (1), 271–280. http://dx.doi.org/10.1007/s10333-015-0496-9.

Kumar, S.S., 2025. Deep learning for rapid crop damage assessment after cyclones. Nat. Hazards 121 (7), 8761–8783. http://dx.doi.org/10.1007/s11069-025-07152-z.

Lateef, L.O., Costa, H., Cabral, P., 2025. Improved integrated framework for flooded crop damage and recovery assessment: A multi-source earth observation and participatory mapping in Hadejia, Nigeria. J. Environ. Manag. 384, 125542. http://dx.doi.org/10.1016/j.jenvman.2025.125542.

Lazin, R., Shen, X., Anagnostou, E., 2021. Estimation of flood-damaged cropland area using a convolutional neural network. Environ. Res. Lett. 16 (5), 054011. http://dx.doi.org/10.1088/1748-9326/abeba0.

Liu, Z., Li, J., Ashraf, M., Syam, M., Asif, M., Awwad, E.M., Al-Razgan, M., Bhatti, U.A., 2024. Remote sensing-enhanced transfer learning approach for agricultural damage and change detection: A deep learning perspective. Big Data Res. 36, 100449.

López-Andreu, F.J., López-Morales, J.A., Erena, M., Skarmeta, A.F., Martínez, J.A., 2022. Monitoring system for the management of the common agricultural policy using machine learning and remote sensing. Electronics 11 (3), http://dx.doi.org/10.3390/electronics11030325.

Meadows, M., Jones, S., Reinke, K., 2024. Vertical accuracy assessment of freely available global DEMs (FABDEM, Copernicus DEM, NASADEM, AW3D30 and SRTM) in flood-prone environments. Int. J. Digit. Earth 17 (1), 2308734. http://dx.doi.org/10.1080/17538947.2024.2308734.

Miao, S., Zhao, Y., Huang, J., Li, X., Wu, R., Su, W., Zeng, Y., Guan, H., Abd Elbasit, M.A.M., Zhang, J., 2023. A comprehensive evaluation of flooding's effect on crops using satellite time series data. Remote Sens. 15 (5), http://dx.doi.org/10.3390/rs15051305.

Nhangumbe, M., Nascetti, A., Georganos, S., Ban, Y., 2023. Supervised and unsupervised machine learning approaches using Sentinel data for flood mapping and damage assessment in Mozambique. Remote Sens. Appl.: Soc. Environ. 32, 101015. http://dx.doi.org/10.1016/j.rsase.2023.101015.

Osisanwo, F., Akinsola, J., Awodele, O., Hinmikaiye, J., Olakanmi, O., Akinjobi, J., et al., 2017. Supervised machine learning algorithms: classification and comparison. Int. J. Comput. Trends Technol. (IJCTT) 48 (3), 128–138. http://dx.doi.org/10.14445/22312803/IJCTT-V48P126.

Pantaleoni, E., Engel, B.A., Johannsen, C.J., 2007. Identifying agricultural flood damage using Landsat imagery. Precis. Agric. 8 (1–2), 27–36. http://dx.doi.org/10.1007/s11119-006-9026-5.

Parker, G.G., 2020. Tamm review: Leaf Area Index (LAI) is both a determinant and a consequence of important processes in vegetation canopies. Forest Ecol. Manag. 477, 118496. http://dx.doi.org/10.1016/j.foreco.2020.118496.

Pasquarella, V.J., Brown, C.F., Czerwinski, W., Rucklidge, W.J., 2023. Comprehensive quality assessment of optical satellite imagery using weakly supervised video learning. In: 2023 IEEE/CVF Conference on Computer Vision and Pattern Recognition Workshops (CVPRW). pp. 2125–2135. http://dx.doi.org/10.1109/CVPRW59228.2023.00206.

Probst, P., Wright, M.N., Boulesteix, A.-L., 2019. Hyperparameters and tuning strategies for random forest. Wiley Interdiscip. Rev.: Data Min. Knowl. Discov. 9 (3), e1301.

Puttinaovarat, S., Saeliw, A., Pruitikanee, S., Kongcharoen, J., Chai-Arayalert, S., Khaimook, K., 2022. Flood damage assessment geospatial application using geoinformatics and deep learning classification. Int. J. Interact. Mob. Technol. (iJIM) 16 (21), 71–97. http://dx.doi.org/10.3991/ijim.v16i21.34281.

Rahman, M.S., Di, L., 2020. A systematic review on case studies of remote-sensing-based flood crop loss assessment. Agric. 10 (4), http://dx.doi.org/10.3390/agriculture10040131.

Rouse Jr., J.W., Haas, R.H., Schell, J.A., Deering, D.W., 1974. Monitoring vegetation systems in the Great Plains with ERTS. In: 3rd ERTS-1 Symposium, Vol. 1, Section A. NASA Goddard Space Flight Center, NASA Paper A20, DOI: —.

Ruiz, L.A., Almonacid-Caballer, J., Crespo-Peremarch, P., Recio, J.A., Pardo-Pascual, J.E., Sánchez-García, E., 2020. Automated classification of crop types and condition in a mediterranean area using a fine-tuned convolutional neural network. Int. Arch. Photogramm. Remote Sens. Spat. Inf. Sci. XLIII-B3-2020, 1061–1068. http://dx.doi.org/10.5194/isprs-archives-XLIII-B3-2020-1061-2020.

Saeed, U., Hussain, M., Hameedullah, Jannat butt, H., Mukhtar, R., Younas, I., Ali, F., Akmal, F., Khan, S., 2024. Development of a spatial framework for flash flood damage assessment and mitigation by coupling analytics of machine learning and household level survey data – A case study of rapid collaborative assessments and disbursement of public funds to the affectees of floods 2022, Punjab Pakistan. Int. J. Disaster Risk Reduct. 108, 104463. http://dx.doi.org/10.1016/j.ijdrr.2024.104463.

Safonova, A., Ghazaryan, G., Stiller, S., Main-Knorn, M., Nendel, C., Ryo, M., 2023. Ten deep learning techniques to address small data problems with remote sensing. Int. J. Appl. Earth Obs. Geoinf. 125, 103569. http://dx.doi.org/10.1016/j.jag.2023.103569.

Salem, Z.E.-S., Arafa, N.A., Abdeldayem, A.L., Youssef, Y.M., 2025. Machine learning-enhanced GALDIT modeling for the Nile Delta aquifer vulnerability assessment in the Mediterranean region. Groundw. Sustain. Dev. 28, 101403.

Shen, X., Wang, D., Mao, K., Anagnostou, E., Hong, Y., 2019. Inundation extent mapping by synthetic aperture radar: A review. Remote Sens. 11 (7), 879. http://dx.doi.org/10.3390/rs11070879.

Shrestha, R., Di, L., Yu, E.G., Kang, L., Shao, Y.-z., Bai, Y.-q., 2017. Regression model to estimate flood impact on corn yield using MODIS NDVI and USda cropland data layer. J. Integr. Agric. 16 (2), 398–407. http://dx.doi.org/10.1016/s2095-3119(16)61502-2.

Tapia-Silva, F.-O., Itzerott, S., Foerster, S., Kuhlmann, B., Kreibich, H., 2011. Estimation of flood losses to agricultural crops using remote sensing. Phys. Chem. Earth 36 (7), 253–265. http://dx.doi.org/10.1016/j.pce.2011.03.005, Recent Advances in Mapping and Modelling Flood Processes in Lowland Areas.

Tran, K.H., Menenti, M., Jia, L., 2022. Surface water mapping and flood monitoring in the Mekong Delta using sentinel-1 SAR time series and Otsu threshold. Remote Sens. 14 (22), 5721. http://dx.doi.org/10.3390/rs14225721.

Wagenaar, D., De Bruijn, K., Bouwer, L., de Moel, H., 2016. Uncertainty in flood damage estimates and its potential effect on investment decisions. Nat. Hazards Earth Syst. Sci. 16 (1), 1–14. http://dx.doi.org/10.5194/nhess-16-1-2016.

Wang, S., Rao, Y., Chen, J., Liu, L., Wang, W., 2021. Adopting "difference-in-differences" method to monitor crop response to agrometeorological hazards with satellite data: A case study of dry-hot wind. Remote Sens. 13 (3), http://dx.doi.org/10.3390/rs13030482.

Wen, C., Sun, Z., Li, H., Han, Y., Gunasekera, D., Chen, Y., Zhang, H., Zhao, X., 2025. Flood mapping and assessment of crop damage based on multi-source remote sensing: A case study of the "7.27" rainstorm in Hebei Province, China. Remote Sens. 17 (5), http://dx.doi.org/10.3390/rs17050904.

Xu, H., 2006. Modification of normalised difference water index (NDWI) to enhance open water features in remotely sensed imagery. Int. J. Remote Sens. 27 (14), 3025–3033. http://dx.doi.org/10.1080/01431160600589179.

Yang, L., Cervone, G., 2019. Analysis of remote sensing imagery for disaster assessment using deep learning: a case study of flooding event. Soft Comput. 23 (24), 13393–13408.